Nanoscale

ROYAL SOCIETY OF CHEMISTRY

PAPER

View Article Online
View Journal | View Issue

Cite this: *Nanoscale*, 2025, **17**, 20351

Templated self-assembly of gold nanoparticles in smectic liquid crystals confined at 3D printed curved surfaces

Mackenzie O'Keefe,†[a] Jane Bernadette Denise M. Garcia, †[b] Abeco J. Rwakabuba,[a] Timothy M. Otchy,[c] Daniel A. Beller *[b] and Mohamed Amine Gharbi *[a]

The fabrication of assembled structures of topological defects in liquid crystals (LCs) has attracted much attention during the last decade, stemming from their potential applications in modern technologies, including photonic devices, tunable optical elements, and soft actuators. A range of techniques can be employed to create large areas of engineered defects in LCs, including mechanical shearing, chemical surface treatment, external fields, or geometric confinement. 3D printing has recently emerged as a powerful technique for fabricating novel patterning topographies, particularly enabling the confinement of LCs in geometries with curved surfaces that are challenging to achieve with conventional microfabrication methods. In this work, we show the advantages of using 3D-printed curved surfaces and controlled anchoring properties to confine LCs and engineer new structures of topological defects, whose structure we elucidate by comparison with a novel application of Landau-de Gennes free energy minimization to the smectic A-nematic phase transition. We also demonstrate the ability of these defects to act as a scaffold for assembling gold (Au) nanoparticles (NPs) into reconfigurable 3D structures. We discuss the characteristics of this templated self-assembly (TSA) approach and explain the relationship between NP concentrations and defect structures, with insights gained from numerical modeling. This work paves the way for a versatile platform for LC defect-templated assembly of functional nanomaterials, with potential applications in energy technology, including next-generation solar cells, tunable metamaterials, and energy-efficient optical devices.

Received 20th June 2024,
Accepted 2nd August 2025

DOI: 10.1039/d4nr02539c

rsc.li/nanoscale

Introduction

The field of nanotechnology has been rapidly growing in the last decade. It has attracted enormous attention, particularly after the discovery of new nanomaterials and the development of diverse ways to manipulate them.[1] The interest also stems from the potential of nanomaterials in producing new applications useful in a wide range of emerging fields, such as energy technology,[2] bioengineering,[3] sensing,[4–6] and optics.[7–9] For this reason, the scientific community has strived to develop new techniques to fabricate and manipulate nanocomposites. One class of these techniques is the top-down approach, which exploits the patterning of bulk materials to organize nanosized structures.[10] Examples include the techniques of photolithography,[11] soft lithography,[12] scanning lithography,[13] nanocontact printing,[14] laser machining,[15] and deposition.[16] Another set of approaches are described as bottom-up methods, in which hierarchical nanostructures are assembled by building upon single atoms and molecules.[17,18] When these two kinds of methods are combined, they give rise to an innovative approach for nanofabrication, known as the templated-self-assembly (TSA) technique,[19] where the top-down helps the bottom-up to create specific structures.[20]

In this work, we propose a novel mechanism of TSA, for which we combine bottom-up self-assembly with top-down patterned templates to create tunable structures of topological defects in liquid crystals (LCs) capable of manipulating nanomaterials. LCs are ordered fluids that have long been of interest because of their reconfigurable properties and their fast response to external stimuli. These materials have also attracted significant attention because of their defects that are easy to engineer and efficient in guiding the assembly of

[a]*Department of Physics, University of Massachusetts Boston, Boston, MA 02125, USA. E-mail: mohamed.gharbi@umb.edu*
[b]*Department of Physics and Astronomy, Johns Hopkins University, Baltimore, MD 21218, USA. E-mail: d.a.beller@jhu.edu*
[c]*Department of Biology and Neurophotonics Center, Boston University, Boston, MA 02215, USA*
† These authors contributed equally to this work.

different classes of functional nanomaterials.[21–29] The use of LCs and their topological defects as a template for bottom-up designs has also opened new avenues for the development of new materials of both fundamental and technological interest. Examples include the fabrication of microlens arrays,[30,31] soft lithography templates,[32] and matrices for nanoparticle (NP) assembly.[33,34]

Recent studies have highlighted the potential of hybrid LC-based systems for advanced optoelectronic applications. The dispersion of metallic NPs such as gold (Au) in nematic LCs has been shown to influence electro-optical properties, lowering threshold voltages and enhancing response times, which can be useful in tunable display technologies and optical switching devices.[35–38] Furthermore, LC-based nanocomposites incorporating graphene derivatives and semiconductor nanomaterials have demonstrated promising applications in energy-efficient optical materials and sensing technologies.[39,40] These advancements emphasize the versatility of LCs in emerging fields and motivate further exploration of their defect structures as functional templates for material assembly.

Our investigation in this study centers on the utilization of the smectic A (SmA) phase, a distinct class of LCs characterized by their lamellar architecture, comprising parallel layers of rod-shaped molecules. This phase can exhibit distinctive defect structures called focal conic domains (FCDs), where the layers wrap around two defect curves, an ellipse, and a hyperbola, each passing through a focus of the other, that contain singularities of layer curvature. These defects offer a valuable foundation for the bottom-up construction of microdevices and functional materials.[41–45] However, their study remains in the shadow of their more extensively researched LC counterparts despite the promising possibilities they present for nanotechnology applications. This reduced attention is because smectics are quite complex to manipulate, and many factors make it hard to fully understand them. Adding nanomaterials makes things even more complicated, possibly changing how smectics behave and affecting the stability of their defects. Hence, our study delves into novel realms by integrating diverse assembly techniques to unravel the complex relationship between nanomaterials and topological defects in smectic LCs.

Several studies have demonstrated a significant correlation between the spatial organization of FCDs and the topography of confining surfaces. These endeavors have been dedicated to refining methodologies for manipulating FCDs, encompassing diverse techniques such as confinement within microchannels or arrays of microposts.[46–48] Another practical approach to assembling FCDs into hierarchical structures is the use of curved surfaces. This avenue enables dynamic manipulation through the modulation of surface geometry's curvature, periodicity, and anchoring conditions.[49–51]

Curvature is a fundamental concept useful in many fields as it imposes specific constraints that can impact molecular self-assembly and the behavior of different types of nanomaterials, including the kinetics of lipid bilayers,[52] the phase behavior of 2D nanosystems,[53] the properties of self-assembled monolayers,[54] the dynamics of Brownian colloids,[55] the interfacial interactions of anisotropic particles,[56] the structure of layered materials,[57,58] and the organization of topological defects in LCs, both passive[59] and active.[60] However, achieving precise control over curvature presents a difficult challenge, particularly when employing classical microfabrication and microfluidic techniques. Experimentally, realizing the desired degree of control over curvature fields can be complex. In many cases, the range of geometries that can be effectively created is restricted to basic shapes like spheres or posts. This inherent limitation underscores the need for innovative approaches and cutting-edge technologies to expand the repertoire of achievable curved structures.

With the recent emergence of the 3D nanoprinting technology, it is now possible to create novel geometries with complex shapes that were not achievable before.[61] This technique opens the doors for new ways to confine LCs and engineer their topological defects, as shown in our previous work with simple 1D undulations.[51] In this study, we focus on more complex 3D printed curved surfaces with double undulations (*i.e.* height oscillations in the X and Y directions) and demonstrate their potential in orchestrating the assembly of FCDs within SmA films, giving rise to entirely novel configurations. Beyond this, we delve into the practical implications of these defect structures by showcasing their role as scaffolds for the precise arrangement of Au NPs. We also discuss the features of this approach and its limitations by analyzing the effect of Au NP concentration on the properties of the smectic film and the organization of FCDs, shedding light on the nuanced interplay between nanomaterials and the complex properties of LCs.

Experimental

3D printed double undulated surfaces

The double undulated geometries used to confine the LC mixture are produced using the raster-scanning direct laser writing (rDLW) system built on a standard resonant-scanning two-photon microscope.[61] This technique can print objects with minimum feature sizes of about $\sim 4 \times 1 \times 1$ μm in the X, Y, and Z directions, respectively. The 3D printed surfaces have undulations in both X and Y directions with a peak-to-peak amplitude of $A = 25 \pm 2$ μm and a wavelength of $\lambda = 300 \pm 2$ μm. The double-undulated surfaces are initially printed with an IP-Dip photoresist (from Nanoscribe, GmbH) and are then transferred into a film of cross-linked polydimethylsiloxane (PDMS from Sigma-Aldrich). The PDMS film is obtained by mixing the elastomer and the curing agent at a ratio of 9 parts to 1 (9 : 1). The mixture is then set under vacuum until almost all the bubbles disappear from the solution. Thereafter, we place the solution into the oven for about an hour at 80 °C until the PDMS becomes solid.

LC cell preparation

The LC mixture studied in this work is obtained by mixing 80 wt% of 4′-octyl-4-cyanobiphenyl (8CB, purchased from Kingston Chemicals Limited that displays a SmA phase at

room temperature) with 20 wt% of 4-pentyl-4-cyanobiphenyl (5CB, purchased from Kingston Chemicals Limited that displays a N phase at room temperature). This LC mixture displays both N and SmA phases with a *N*-isotropic (I) transition temperature at T_{NI} = 39.3 ± 0.2 °C and a SmA–N transition temperature at T_{SN} = 16.4 ± 0.4 °C. This mixture is helpful for the preparation of samples at room temperature, with and without NPs, because the N is less viscous than the SmA. The 8CB/5CB mixture is then confined between the PDMS film with the double-undulations and a coverslip treated with polyvinyl alcohol (PVA from Sigma-Aldrich). The thickness between the peaks of the undulations and the flat coverslip is estimated to be around $h \approx 5 \pm 2$ μm. The anchoring of the LC mixture is perpendicular in contact with the PDMS and planar at the PVA-treated coverslip. These anchoring conditions induce a "hybrid texture" in the LC film responsible for the formation of defects in the N and SmA phases.

Dispersion of gold (Au) nanoparticles (NPs) in the LC

Spherical Au NPs of diameter 20 nm stabilized with citrate ligands in an aqueous solution (purchased from NNCrystal) are dried under a slow airflow to eliminate water. The dry NPs are then dispersed in an ethanol solution and added to the 5CB/8CB mixture. The solvent was then evaporated under a slow airflow at 60 °C overnight. Finally, the samples were vacuum-dried at the same temperature for one hour to eliminate any residual solvent. The samples were used immediately after the dispersion of NPs to avoid the formation of big aggregates. To validate the anchoring properties of the NPs, we employed a method involving the dispersion of a monolayer of these NPs onto the surfaces of two glass slides. The monolayer of NPs acts as a coating layer, similar to those typically used to control LC alignment in conventional cells. Following this, we introduced the LC mixture between the two glass slides and analyzed its texture using polarizing microscopy during its transition into the nematic phase. We specifically focused on the nematic phase as a reference, as its textures are well-characterized for different anchoring conditions, including planar, homeotropic, and hybrid alignments. These examinations revealed that the LC exhibited a planar anchoring at the surface of the glass slides coated with NPs, confirming that the NP surfaces impose a planar orientation on the LC molecules.

Characterization

To characterize the 3D shape of the PDMS films with undulations and measure their peak-to-peak amplitude and wavelength, we used the Zeta-20 benchtop optical profiler. The LC mixture is studied under an upright optical polarizing microscope (Leica DM6 M) in transmission mode equipped with a temperature controller (Instec TS102-mK2000A) that has a precision ~0.1 °C. This microscope is capable of collecting and comparing data in different modes simultaneously (bright field, polarized, and dark field). It is also equipped with an automated *XYZ* stage useful for 3D imaging and measurements. All images were recorded with a high-resolution digital camera (Leica DMC 5400).

Theory and numerical methods

Multi-step Landau-de Gennes free energy minimization

The Landau-de Gennes (LdG) free energy utilizes a second-order traceless and symmetric tensorial order parameter, Q_{ij}, which contains information regarding the director $\tilde{n}$ and the N degree of order, S.[62,63] The ijth element of the Q-tensor is given by, in the uniaxial limit, $Q_{ij} = \frac{3}{2}S\left(n_i n_j - \frac{1}{3}\delta_{ij}\right)$. In the absence of an external field, the LdG free energy has three components: phase free energy, distortion free energy, and surface free energy,

$$F_{LdG} = \int dV(f_{phase} + f_{dist}) + \int dA f_{surf}. \quad (1)$$

In (1), the bulk free energy density components are:

$$f_{phase} = \frac{1}{2}AQ_{ij}Q_{ji} + \frac{1}{3}BQ_{ij}Q_{jk}Q_{ki} + \frac{1}{4}C(Q_{ij}Q_{ji})^2, \quad (2)$$

and

$$f_{dist} = \frac{1}{2}L_1\frac{\partial Q_{ij}}{\partial x_k}\frac{\partial Q_{ij}}{\partial x_k} + \frac{1}{2}L_2\frac{\partial Q_{ij}}{\partial x_j}\frac{\partial Q_{ik}}{\partial x_k} + \frac{1}{2}L_3 Q_{ij}\frac{\partial Q_{kl}}{\partial x_i}\frac{\partial Q_{kl}}{\partial x_j}. \quad (3)$$

In the uniaxial limit, the distortion free energy can be written in terms of the Frank elastic constants:

$$f_{dist}^{FO} = \frac{1}{2}K_1(\nabla\cdot\hat{n})^2 + \frac{1}{2}K_2(\hat{n}\cdot(\nabla\times\hat{n}))^2 + \frac{1}{2}K_3|\hat{n}\times(\nabla\times\hat{n})|^2, \quad (4)$$

where K_1, K_2 and K_3 are the splay, twist and bend parameters, respectively. In terms of the elastic parameters in eqn (3), $L_1 = 2(-K_1 + 3K_2 + K_3)/27S_0^2$, $L_2 = 4(K_1 - K_2)/9S_0^2$, and $L_3 = 4(K_3 - K_1)/27S_0^3$. We note that close to the SmA–N phase transition, the twist and bend parameters diverge since these two distortions are disallowed in the SmA phase.[63]

For the surface free energy contribution, we consider two types of alignment: homeotropic (perpendicular) anchoring and degenerate planar anchoring. For surfaces with homeotropic anchoring, we employ a Rapini–Papoular surface free energy density,[64,65]

$$f_{surf}^{\perp} = \frac{1}{2}W_0(Q_{ij} - Q_{ij}^0)^2, \quad (5)$$

where W_0 gives the anchoring strength, and Q_{ij}^0 gives the preferred surface tensorial order parameter, $Q_{ij}^0 = \frac{3}{2}S_0\left(\nu_i\nu_j - \frac{1}{3}\delta_{ij}\right)$, where $\tilde{\nu}$ is the surface normal. For degenerate planar anchoring, we follow the Fournier–Galatola formulation for the surface free energy density,[66]

$$f_{surf}^{\parallel} = W_1\left(\tilde{Q}_{ij} - \tilde{Q}_{ij}^{\perp}\right)^2 + W_2\left(\tilde{Q}_{ij}\tilde{Q}_{ji} - \left(\frac{3}{2}S_0\right)^2\right)^2. \quad (6)$$

In the Fournier–Galatola formulation, $\tilde{Q}_{ij} = Q_{ij} + \frac{1}{2}S_0\delta_{ij}$, and $\tilde{Q}^{\perp}_{ij} = P_{ik}\tilde{Q}_{kl}P_{lj}$, with projection operator $P_{ij} = \delta_{ij} - \nu_i\nu_j$ making $\tilde{\boldsymbol{Q}}^{\perp}$ the projection of $\tilde{\boldsymbol{Q}}$ onto the (local tangent) plane of the substrate.

While the LdG framework models the N phase and does not account for the presence of smectic layers, we perform numerical modeling in the N phase close to SmA–N transition as in previous works,[67,68] utilizing smectic-like elasticity $K_2 > K_1$ and the N director field normal to layer configurations of nonzero-eccentricity FCDs.

In the first application of LdG free energy minimization, we consider a configuration of four converging FCDs in the smectic with eccentricity $e = 0.5$, following the eccentricity of the FCDs observed in prior work,[51] with the ellipses parametrizing the FCDs placed on the flat surface where we impose degenerate planar anchoring. The point of convergence of the hyperbolae of the FCDs corresponds to the same (x, y)-value as the position of the trough of the double undulated surface, *i.e.*, where the LC thickness is minimum. Homeotropic anchoring is imposed on the double undulated surface. To obtain a complete picture of the director field in the entire LC, we perform a N free energy minimization on the sites outside the FCDs, constrained by the fixed director field inside the FCDs.

Having obtained the N director field close to the SmA phase in the entire LC, we perform a second free energy minimization now for all the points in the LC to determine the defect evolution going into the N phase. Since we have been considering the N phase close to T_{SN}, we use $K_2 = 2K_1$, reflecting the divergence of the twist distortion parameter in the SmA phase. Finally, to complete the defect evolution into the N phase, we perform a third relaxation with equal elastic constants to obtain a configuration deep in the N phase.

Numerical details

Simulations for defect evolution were performed in a 450 × 450 × 40 lattice, with lattice spacing equivalent to 4.5 nm through a finite difference relaxation method.[69] Material constants used for the phase free energy in (1) were $A = -0.172 \times 10^6$ J m^{-3}, $B = -2.12 \times 10^6$ J m^{-3} and $C = 1.73 \times 10^6$ J m^{-3}, which gives $S_0 = \left(-B + \sqrt{B^2 - 24AC}\right)/6C \approx 0.533$. Defects are marked where the N scalar order parameter $S < 0.8S_0$. In the three-constant distortion free energy, we use the elastic constants for 8CB given in ref. 70, with $K_1 = 8 \times 10^{-12}$ N, $K_3 = 8 \times 10^{-12}$ N and $K_2 = 2K_1$ for the first two relaxation steps. In the third relaxation step, $K_1 = K_2 = K_3 = 8 \times 10^{-12}$ N. For all the relaxation steps, homeotropic anchoring was imposed on the double undulated surface with anchoring strength $W_0 = 5 \times 10^{-3}$ J m^{-2}, and degenerate planar anchoring on the flat surface with anchoring strength $W_1 = 1.067 \times 10^{-1}$ J m^{-3} and $W_2 = 0$. These values for anchoring are consistent with the experimental ratio of anchoring extrapolation lengths to system size, $\xi_{\parallel}/h = 10^{-2}$ and $\xi_{\perp}/h = 10^{-1}$, where $h \sim 10^{-5}$ m. Simulations for NP assembly were performed in a 75 × 75 × 40 lattice with the same lattice spacing as the defect evolution simulations. All material constants and surface anchoring constants are consistent with the defect evolution simulations. For elastic constants, we chose $K_2 = 2K_1$ for the near-smectic scenario, and the anchoring strength on the surface of the NPs is $W_{NP} = 2.4 \times 10^{-4}$ J m^{-2}, with the ratio of the anchoring extrapolation length and NP radius $\xi_{NP}/r_{NP} \sim 10$, consistent with the weak anchoring limit for the NP surface.

Results and discussion

Confinement of the LC mixture at 3D printed curved surfaces

We confine a 5CB/8CB mixture at a ratio of 20/80 by weight percent (wt%), between a PDMS film that presents undulations in both X and Y directions and a coverslip treated with PVA. Fig. 1 shows the optical image obtained in transmission mode and the 3D profile measured using an optical interference profilometer of the PDMS film used to confine the mixture. The PDMS film was replicated from a 3D printed master mold that has undulations with peak-to-peak amplitudes of $A = 25 \pm 2$ μm and a wavelength of $\lambda = 300 \pm 2$ μm. The anchoring of the 5CB/8CB mixture is homeotropic (perpendicular) at the PDMS surface and planar at the PVA-coated coverslip, resulting in a hybrid alignment of the LC film. This behavior is consistent with the known anchoring properties of individual 5CB and 8CB LCs in contact with these surfaces. Our experimental observations confirm that the mixture exhibits the same anchoring characteristics, maintaining homeotropic alignment at the PDMS interface and planar alignment at the PVA-coated coverslip. This alignment is further validated by analyzing the texture and defect structure of the mixture in the flat regions of the sample, where the LC film is uniformly confined in both the nematic and smectic phases. While the anchoring and resulting textures may be more complex in the undulated regions, this analysis provides a clear reference for the boundary conditions governing LC alignment in our system.

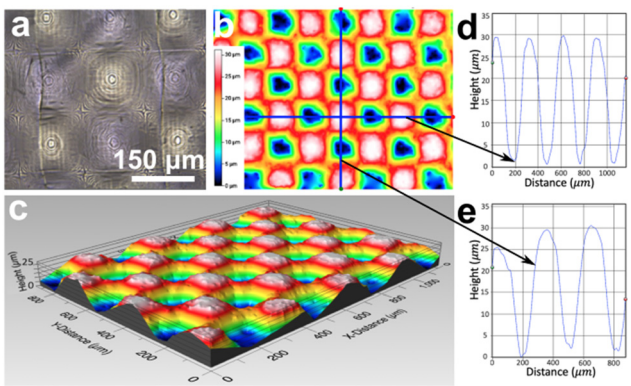

Fig. 1 Characterization of the curved PDMS surface used to confine the LC mixture. (a) Optical image of the PDMS film. (b) Interferogram of the PDMS surface. (c) 3D reconstruction of the PDMS surface. Profile of the surface in the X (d) and Y (e) directions. The double undulations have peak-to-peak amplitudes of $A = 25 \pm 2$ μm and a wavelength of $\lambda = 300 \pm 2$ μm.

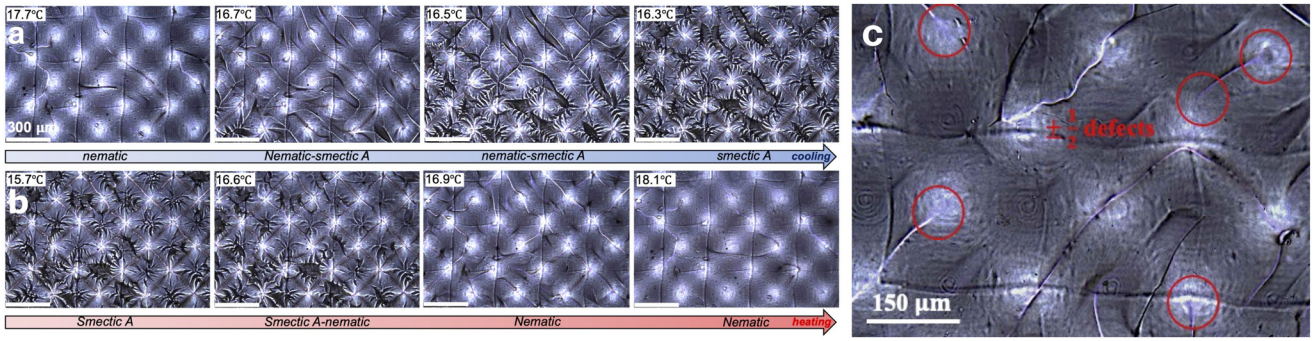

Fig. 2 Behavior of the LC mixture near the N–SmA phase transition. Optical images showing the textures of the LC mixture during cooling from the N to the SmA phase (a) and during heating from the SmA to the N phase (b). The images illustrate the formation and arrangement of disclinations and FCDs during the phase transition. In the smectic phase, the disclinations appear as straight lines oriented along the lattice directions of the surface's square lattice (diagonal to the image edges), and passing through the sites of minimum thickness in the liquid crystal, where they appear to intersect. In contrast, the vertically and horizontally aligned lines visible in all figures, are artifacts from the 3D printing process. (c) A closer view of a typical N-phase defect configuration, with red circles marking some examples of disclination endpoints.

The 5CB/8CB system presents an isotropic phase at temperatures above T_{NI} = 39.3 ± 0.2 °C, a nematic (N) phase between T_{NI} and T_{SN} = 16.4 ± 0.4 °C, a smectic A (SmA) phase between T_{SN} and T_{CS} = 5.4 ± 0.2 °C, and a crystal phase below T_{CS}. Fig. 2 shows the bright field optical images obtained in transmission mode of the mixture near the N–SmA phase transition.

We used a mixture of 5CB and 8CB instead of pure 8CB because the latter presents a strong viscosity at room temperature, which could be a disadvantage with Au NPs. We found that adding a small amount of 5CB to the 8CB preserves the N and SmA mesophases, but modifies their phase transition temperatures, leading to a N phase at room temperature and a SmA phase at lower ones.[71] We also noticed that the phase diagram of this system is very sensitive to the addition of 5CB. We tested different ratios and found the optimal concentration to be 20/80 wt%, because higher 5CB concentrations suppress the SmA phase.

Characterization of the defect structure in the LC

We begin our characterization by analyzing the texture of the LC mixture near the N–SmA phase transition and comparing the patterns of LC defects at flat and double-undulated surfaces. The goal of this analysis is to understand the effects of curvature and thermal history on the structure and assembly of topological defects in the N and SmA phases. When cooling the mixture from the isotropic to the N phase, we observe the appearance of disclination lines that tend to shrink over time if the LC is maintained in its N phase. The energetic cost of these defect lines gives them an effective line tension,[62] so the LC tends to shrink and eliminate them over time in order to minimize its free energy. However, some defects persist indefinitely in the double undulated confinement, suggesting that curvature is responsible for creating and stabilizing defects in NLCs. Disclinations in the N phase typically span a few unit cells of the surface undulation, with distinct endpoints apparent under bright-field microscopy (Fig. 2c) and sometimes distinguishable in polarized optical microscopy as meetings of two dark schlieren brushes (Fig. 4c), consistent with profiles of 2D defects with winding number ±1/2 where the disclinations meet the planar surface.

Boojums, or surface point defects of ±1 winding, are also seen in the N phase under polarized optical microscopy as intersections of four schlieren brushes, as shown in Fig. 4c. In some instances, the defect point itself was optically apparent (Fig. S4); however, the complexity of the system made it challenging to obtain high-quality images of these defects. Even though boojums and disclination endpoints likely all occur at the flat surface, due to its degenerate planar anchoring, there is a clear correlation between the horizontal positions of these surface defects and the geometry of the homeotropic-anchoring, double undulated surface, which we explore in detail below. The interplay between curvature effects, thermal history, and confinement geometry plays a critical role in determining the stability and morphology of these defect structures. While our images clearly demonstrate the presence of ±1/2 endpoint defects in the N phase, the limited resolution of standard microscopy techniques prevented us from confidently distinguishing between +1/2 and −1/2 charges. More advanced imaging techniques will be required to provide a clearer and more direct visualization of these topological defects, which will be the focus of future studies.

As the system is cooled toward the SmA phase, additional disclinations emerge at well-defined locations, forming a periodic pattern. Specifically, the density of disclinations increases during the N–SmA phase transition, organizing into parallel and perpendicular lines that intersect near the peaks of the undulations, locations where the LC thickness is minimum. This periodic arrangement is particularly evident in the image captured in the smectic phase at 16.3°C (Fig. 2a). Additionally, FCDs of different sizes emerge, forming hierarchical assemblies of larger and smaller defects around these disclinations. This process is reversible: disclinations in the N phase re-emerge at approximately the same locations after the system is

heated and cooled through many cycles, as shown in Fig. 2b, exhibiting a form of geometric memory across the phase transition.[67]

To better understand the formation of defects in the SmA phase and the role of the 3D printed surface, we characterized the structure of the defects as a function of the confining surface profile. Fig. 3a shows a typical optical image of the SmA confined at a double-undulated surface. From above, each FCD appears as an ellipse of high eccentricity, distinguishing these defects as elliptic-hyperbolic FCDs as opposed to the zero-eccentricity toric FCDs.[63] Fig. 3b is the corresponding 3D reconstruction of the smectic texture obtained by scanning the sample along the *z*-axis. These measurements indicate that the disclinations form a cross-hatch grid of lines that appear to intersect near the coverslip, above the crests in the double-undulated surface. We are unable to determine the *z*-separation of the defects, which means we cannot confirm if they are really intersecting or not. The FCDs assemble in groups resembling petals of a flower, centered at these disclination intersection sites. These results confirm the correlation between the morphology of the confining surface and the assembly of defects.

Additionally, we measured the number of petals present in the flower patterns and found that they all have between 4 and 6 petals, as shown in the histogram of Fig. 3d. However, the majority of the flowers present 5 petals. We believe that the variability in petal numbers is linked to the thickness of the smectic film between the crest of the double undulation and the coverslip's surface, as FCDs' size and number are sensitive to this parameter. Since the thickness of our samples varies slightly, which is challenging to regulate experimentally, the number of petals may differ from one region to another, as seen in Fig. 3a, from the bottom right to the top left. These results suggest that further control over FCD assembly structures may be obtainable by systematically varying parameters that we do not investigate here, including sample thickness and the amplitude and wavelength of the double undulations.

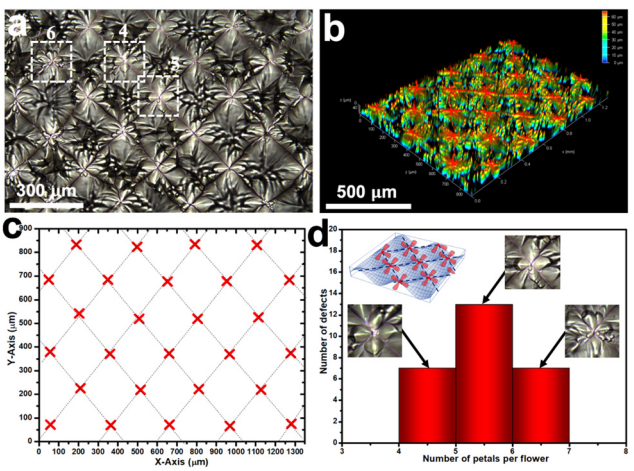

Fig. 3 Characterization of the defect structure of the SmA LC confined at a 3D printed double undulated surface. (a) Optical image of the smectic patterns showing the formation of parallel and perpendicular defect lines that appear to intersect each other near the peaks of the undulations. The image also shows the formations of flower patterns of FCDs around the disclinations. The three highlighted boxes here indicate the locations of the flower patterns used as insets in (d), showing examples of smectic flowers with different numbers of petals. (b) 3D reconstruction of the defect assembly in the SmA obtained by scanning the sample along the *Z* axis. (c) Measure of the smectic flower center positions. The dashed lines are virtual lines that indicate the structure of disclinations connecting the positions of the flower centers. (d) Histogram of the number of petals per smectic flower. Inset images show examples of flowers with four, five, and six petals. The inset sketch indicates the position of these flowers with respect to the double undulated PDMS surface.

In order to better understand the LC defect configurations in the double-undulated confinement, and their transformations at the SmA–N phase transition, we turn to Landau-de Gennes (LdG) numerical modeling. Typically, LdG numerical relaxation with random initial conditions models a quench from the isotropic to the nematic phase (I–N).[69] Here, to model the SmA–N transition, we conduct a novel, multi-step application of LdG free energy minimization, which accounts for the initial FCD arrangement in the SmA phase and the changing elasticity in the N phase close to T_{SN}. The final nematic defect configuration strongly depends on the initialization of the director field, and we explore this dependence in more detail in the SI in Fig. S2 and S3.

As part of our model's initial condition, we assume an arrangement of four elliptic-hyperbolic FCDs in each unit cell of the double-undulation (Fig. 4a). We model the four-petal configuration because it is the most symmetric packing of non-zero eccentricity FCDs observed in the experiment, as its four-fold rotational symmetry matches that of the double-undulated surface at the center of the flower. Configurations of five or six petals would break this registry with the surface, introducing many more degrees of freedom in the construction of the FCD configuration. Our goal in this work was not to match the FCD configuration in experiments (which includes many more FCDs, besides the petals of the flowers, than we have the computational power to simulate) but to model a small number of FCDs whose orientations relative to the surface undulations are similar to those of the experiment, *i.e.*, with hyperbolas oriented toward the flower centers. As the main focus of our simulations is to model N-phase defect configurations following the SmA–N transition, we leave for future work the much more challenging task of accurately replicating the experimentally observed FCD configurations.

With the N director field within the FCDs known analytically,[63] we first relax the director field only outside of the FCDs, and with twist elastic constant larger than the splay elastic constant, $k_2 \equiv K_2/K_1 = 2$, to approximate the smectic configuration.[72,73] Starting from this FCD director configuration, we perform a second relaxation at $k_2 = 2$ over the entire domain to produce a modeled N configuration just above T_{SN}. Finally, a third relaxation with equal elastic constants evolves the system into a metastable state deep inside the N phase. This method extends the numerical approach developed in ref.

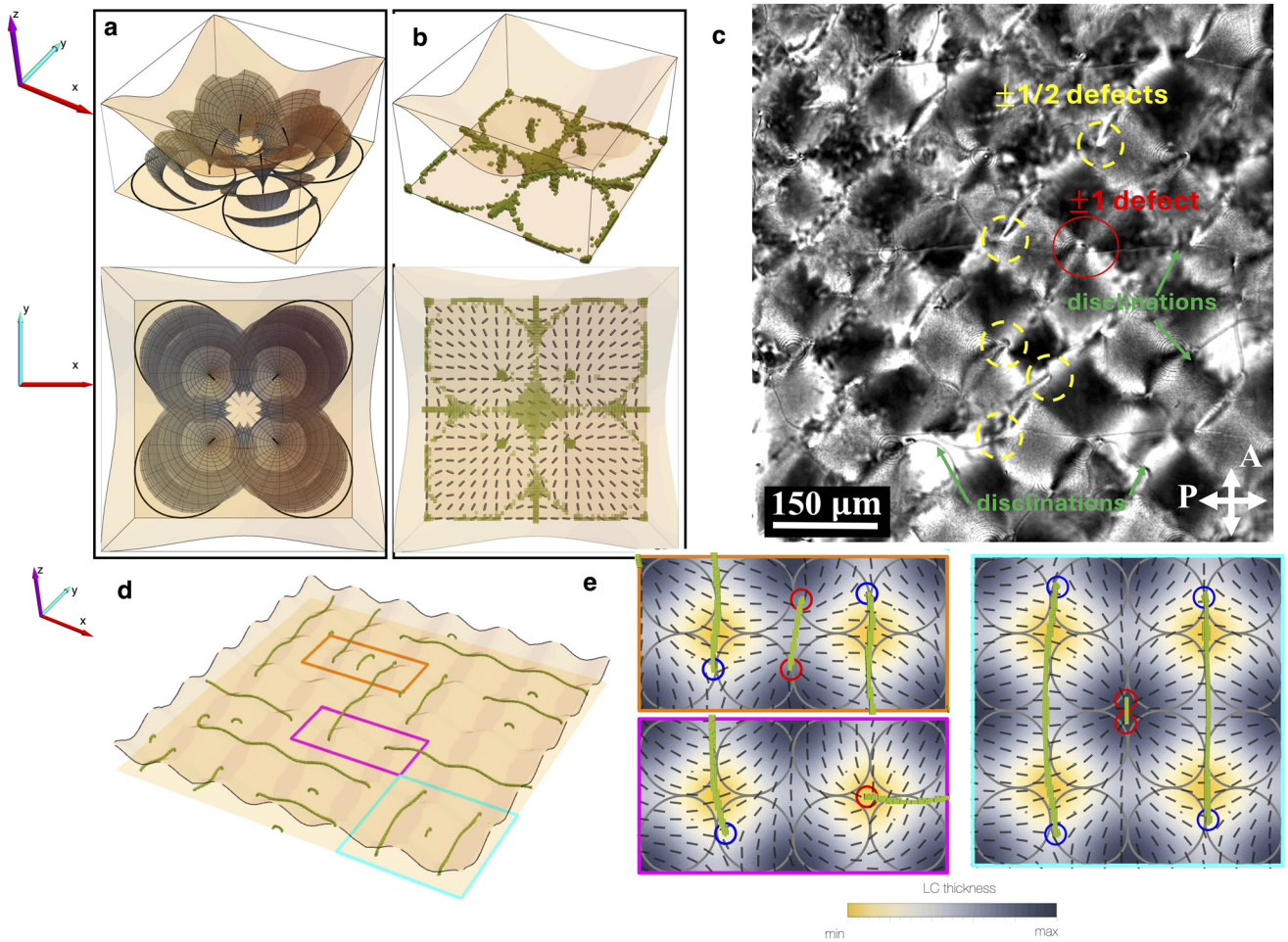

Fig. 4 Numerical modeling of defect evolution in double-undulated confinement at the SmA-to-N phase transition. (a) Schematic of the positions of the FCDs used in the first application of the LdG free energy minimization. (b) Defects (green) arising after the first LdG relaxation, in which the director is held fixed inside the FCDs. Black rods represent the director field on the flat surface with degenerate planar anchoring. (c) Polarized optical microscopy image of a typical experimental configuration in the nematic phase, with some of the several disclination lines labeled. Disclination endpoints (examples circled in yellow) appear as the intersection of two dark brushes, whereas point defects (circled in red) appear as the intersection of four dark brushes in the schlieren texture. (d) A metastable configuration of disclination lines after final application of LdG free energy minimization, modeling a state deep in the N phase. (e) Three zoomed-in views of three different subsets of defects boxed in (d). Grey ellipses show the locations of the FCDs used in the first application of LdG free energy minimization. The flat surface is colored by the thickness of the LC bulk. Defect endpoints intersecting the flat surface are encircled with blue (–1/2 winding) and red (+1/2 winding) circles. Point-like +1 defects are visible in their split-core forms as a short disclination half-loops with winding number +1/2 at both endpoints.

67 and 73 for modeling the SmA–N transition with an initial state of toric focal conic domains.

At the end of this multi-step energy minimization procedure, we find nematic configurations containing several disclination lines, whose endpoints lie on the flat (degenerate planar anchoring) surface, when we use $k_3 \equiv K_3/K_1 = 1$. These disclinations share some important features with the disclination lines observed in the nematic phase under bright-field optical microscopy (Fig. 2): they may extend over only a small portion of one unit cell of the surface undulation, or over a few adjacent unit cells; they may exhibit sharp bends; and they are arranged irregularly in any of a large number of possible metastable configurations. An example of such a metastable array is shown in Fig. 4d and e. This highly multistable scenario is in stark contrast with the disclination configuration arising under single-undulated confinement, as investigated experimentally in[51] and numerically in the SI (Fig. S1), where the NLC exhibits a unique stable state with parallel, straight disclinations.

The multistability in our system is a consequence of the double-undulated surface geometry, and is observed both in our multi-step SmA–N model and in the single-step I–N LdG relaxation from random initial conditions (Fig. S2). However, the disclination configurations predicted by the two LdG relaxation approaches are qualitatively different: Typical disclinations are more curved in the single-step I–N model than in the multi-step SmA–N model (Fig. S2), even though the final step of the latter approach uses the same elastic constants as the

former. In the SI, we separately investigate the dependence of the final disclination configuration on the initial elastic constant ratios and on the initial director field, demonstrating that both aspects of our multi-step method are important for the results presented here.

Furthermore, the curvature of the double undulated surface geometry influences the local structure of nearby defects. Disclination line endpoints where the N director has −1/2 winding lie close to saddle points (median thickness) of the double undulated surface, whereas those with +1/2 winding mostly lie opposite the undulation troughs, where LC thickness is minimum. This indicates a relationship between surface defect "charge" at one interface and the Gaussian curvature of the nearby opposite surface, extending a connection between surface curvature and defect charge known previously from in-surface[74,75] and bulk[76] behaviors. The relationship between defect endpoint charge and local surface Gaussian curvature shows an interesting history-dependence (SI Fig. S3), with a pronounced clustering at strongly positive and strongly negative curvatures under our multi-step SmA–N model, in contrast with a broader range of curvature values under our I–N model at the same final set of elastic constants. Although we were unable to systematically quantify this correlation in our experiments due to limitations in resolving defect charge, we observe that defect endpoints frequently localize near the crests and troughs of the undulated surface, suggesting a possible geometric influence consistent with our simulation results.

Our modeling also sheds light on the boojums, showing that their locations and types are strongly influenced by the surface curvature and thermal history. Using the SmA–N model with k_3 = 1, in the final nematic state we observed +1 boojums on the flat surface. These defects appear as split-core short disclination lines,[77] such as the central defect in the right-hand panel of Fig. 4e. Boojums arising under these conditions in the SmA–N simulations are found to be of the diverging positive type, $+1_D$, equivalent to half of a radial hedgehog. Under these conditions, our simulations do not produce the other type of +1 boojum, the converging $+1_C$ type, nor the −1 boojum, in contrast to previous simulations of toric FCD packings at the SmA-to-N phase transition[67] where all three types were observed. The influence of the SmA history is revealed when we repeat the simulation with a simple I–N quench from random initial conditions, in place of our multi-step SmA–N procedure, as we then obtain boojums of $+1_C$ type as well as $+1_D$, as shown in Fig. S2a.

To explore the thermal history dependence of our multistable N-phase defect configurations, we next examine the result of an I–N quench. While we see coexistence of boojums and disclination lines as in the SmA–N transition, we find experimentally that boojums arising after the I–N quench have a more regular arrangement, appearing in a quasi-checkerboard pattern opposite the crests, troughs, and saddle points of the double undulated surface (Fig. 5a). Under polarized optical microscopy, these surface defects appear as the intersection of four dark brushes in the schlieren texture. The dis-

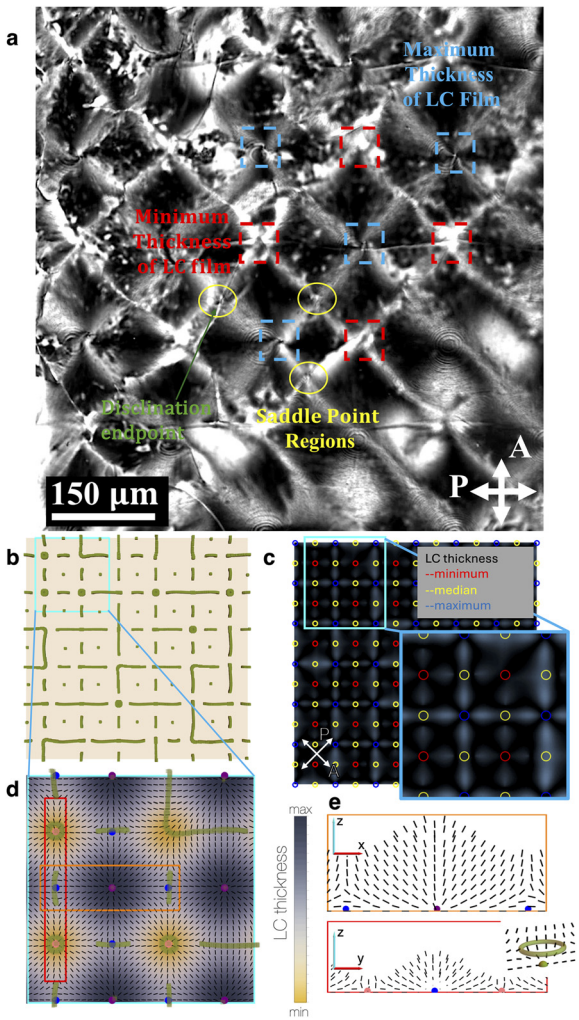

Fig. 5 Coexistence of disclination lines with a quasi-checkerboard of surface point defects in the nematic phase. (a) Experimental polarized optical microscopy image of array of ±1 defects in the nematic from an isotropic quench indicated by the presence of the intersection of four dark brushes in the schlieren structure located at the minimum, maximum and median liquid crystal thickness. Disclination line endpoints of ±1/2 winding are also seen as the intersection of two dark brushes in the schlieren texture (green), found at median liquid crystal thickness. (b) Coexistence of disclination lines and ±1 surface boojums as obtained from LdG free energy minimization simulating an isotropic-nematic quench with $k_2 = K_2/K_1 = 3$ and $k_3 \equiv K_3/K_1 = 4$ with the defects shown as green points and lines. ±1 defects appear as split-core short disclination lines. (c) Simulated polarized image of the defect configuration in (b), and a zoomed-in inset of a set defects shown in the schlieren texture. Point-like defects appear as the intersection of four dark brushes in the simulated schlieren structure, whereas ±1/2 defects appear as the intersection of two dark brushes in the simulated structure. Also marked are regions of minimum (red), maximum (blue) and median (yellow) liquid crystal thickness. (d) Zoomed-in view of a subset of defects boxed in (b). Black rods show the director field on the flat surface. Marked are centers of the split-core −1 defects (blue dots), and +1 defects (pink and purple dots). The flat surface is colored by the LC bulk thickness. (e) Director field cross sections showing the tilt directions of the boojums. Pink dots correspond to +1-diverging type boojums and purple dots correspond to +1-converging type boojums. Inset shows more closely the structure of the +1-converging defect type, which is composed of a +1-diverging surface point defect together with a disclination loop of hedgehog charge −1.

clination lines coexisting with these boojums have endpoints that similarly lie at the extrema of LC thickness.

In our numerical modeling, we find that we can reproduce the quasi-checkerboard pattern of boojums when we set $k_2 = 3$ and $k_3 = 4$ in the nematic state, although it is unclear why such high ratios are needed. Here, we find that the standard I–N quench model provides a better match than our SmA–N procedure to the experimental I–N observations of Fig. 5a. As shown in Fig. 5b and c, the I–N model produces a quasi-checkerboard configuration of boojums, appearing as split-core short disclinations, in coexistence with many disclination lines of length on the order of the surface periodicity. In contrast, with our multi-step SmA–N modeling approach, with the same elastic constants used in the first and second steps, we find an absence of disclination lines, and instead obtain a perfect checkerboard of boojums with alternating ±1 winding (Fig. S2c), which we did not observe experimentally. (The third step of the SmA–N procedure, with the elastic constants set equal, does not qualitatively change the defect configuration.) The boojums of Fig. 5b include $+1_C$, $+1_D$, and -1 boojums respectively located at minimal, maximal, and median liquid crystal thickness (Fig. 5c and d). The form of $+1_C$ boojums in simulations exhibits a surprising compound structure, consisting of a short split-core disclination line with +1/2 winding at each endpoint (equivalent to a $+1_D$ boojum) accompanied by a disclination loop of hedgehog charge −1 nearby in the liquid crystal bulk (Fig. 5e). In contrast, $+1_D$ boojums consist only of the short, split-core disclination structure, with no accompanying defect loop. The −1 boojums appear as somewhat longer split-core disclination lines.

Wherever boojums appear, both in the I–N quasi-checkerboard of Fig. 5 and in the more disordered SmA–N configurations of Fig. 4c and d, their locations are determined by the geometry of the double-undulated surface. Specifically, boojums strongly prefer to sit opposite Gaussian curvature extrema of the same sign as the boojum's winding number. The director field in the flat surface around these boojums consistently exhibits +1 winding at locations opposite the crests and troughs of the undulated surface, where Gaussian curvature is most strongly positive, and −1 winding at locations opposite the saddle points of the undulated surface, where Gaussian curvature is most strongly negative. This trend agrees with the coupling of winding number sign to Gaussian curvature that we observed in disclination line endpoints in Fig. 4. Moreover, when $+1_D$ boojums are present, these are always found under regions of maximum liquid crystal thickness, whereas $+1_C$ boojums are found under regions of minimum liquid crystal thickness. For −1 boojums split into short disclination lines with endpoints of winding number −1/2, the minimum of Gaussian curvature coincides with the defect's center, rather than either of its endpoints, where the Gaussian curvature is slightly less negative.

Directed assembly of Au NPs *via* engineered defects in the smectic LC

It is known that topological defects in LCs present strong trapping sites for nanomaterials.[21,22,29,33,34] In this section, we explore the possibility of using defects assembled at curved geometries as a scaffold to organize NPs into reconfigurable ordered structures. We used Au NPs of nominal diameter 20 nm, stabilized with citrate ligands and dispersed in the LC mixture at different concentrations. The presence of ligands at the NP surfaces helps them to disperse uniformly in the LC and prevents them from forming large aggregates. The ligands also promote degenerate planar anchoring of the LC molecules at the surfaces of the NPs. In this section, we focus on the SmA phase because of its highly organized defects. Our motivation is to investigate whether NPs could conform to the structure of LC defects.

We examined various concentrations of Au NPs, ranging from 0.02 wt% (~0.00285 volume percent (vol%)) to 0.2 wt% (~0.0286 vol%). We first establish the behavior of our NPs in uniformly confined SmA films with hybrid alignment, where both interfaces are planar. The goal was to verify if NPs used in this study could interact with self-assembled FCDs, as previously demonstrated with other types of NPs.[28,41] Our findings show that the NPs are attracted to the FCDs. This was confirmed by observing the sample near the N–SmA phase transition (Fig. S5). These results demonstrate the potential of smectic defects in attracting the NPs and manipulating their organization, suggesting a similar mechanism in undulated cases.

Fig. 6 shows optical images of the samples prepared at different NP concentrations: 0.02 wt% (~0.00285 vol%), 0.04 wt% (~0.00571 vol%), and 0.2 wt% (~0.0286 vol%). Our results indicate that the presence of a low concentration of

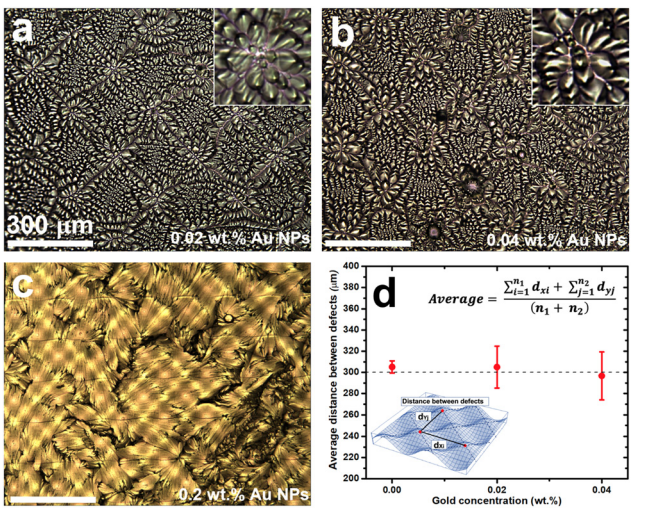

Fig. 6 Texture of the SmA as a function of Au NP concentration obtained *via* bright-field microscopy. Defect structures of the SmA with 0.02 wt% (a), 0.04 wt% (b), and 0.2 wt% Au NPs (c). When the concentration of NPs is high (c), the disclinations and FCDs disappear. This is because the NPs migrate to the boundaries and change the anchoring properties of the SmA from hybrid to planar. (d) Average distance between defect intersections as a function of Au NP concentration. The inset sketch and formula show how we measured the average distance between defect intersections.

NPs doesn't affect the structure of disclinations and FCDs in the smectic film, as shown in Fig. 6a. For Au NP concentration of 0.02 wt%, the average distance between the defect lines, obtained by averaging the distances d_X and d_Y between the defect intersections in both X and Y directions (see inset of Fig. 6d), is $d \approx 305 \pm 20$ μm, compared to $d \approx 305 \pm 6$ μm for samples without NPs. Since FCDs and disclinations can act as strong trapping sites for NPs—a mechanism consistent with our findings in flat samples—these observations suggest that curvature-induced FCDs and disclinations may serve as effective templates for guiding the assembly of NPs. However, directly confirming NP accumulation within smectic defects remains challenging due to the high defect density, which results in NPs being distributed across multiple sites, making their localization difficult to resolve. Additionally, limitations in optical resolution and contrast further hinder the ability to distinctly visualize NPs within the defect structures. To provide more conclusive evidence, further measurements may be necessary, such as scanning electron microscopy (SEM). However, SEM is not compatible with our experimental system, as the required vacuum environment and sample preparation could disrupt the smectic phase and significantly alter the defect structures. While alternative smectic materials with better SEM compatibility could be explored, switching to a different system may fundamentally change the study, potentially altering both the defect configurations and NP interactions.

When the concentration of NPs is increased to 0.04 wt%, these defects continue to form ordered structures but with some deformations in their arrangements, as shown in Fig. 6b. The flower patterns of FCDs that form around the disclinations become less defined with a larger number of petals. The average distance between the disclination intersection points decreases, and its standard deviation increases ($d \approx 296 \pm 23$ μm). This result reveals that at certain concentrations, the NPs can distort the regular defect structures of the smectic obtained without or with low NP concentrations (see Fig. 6d).

When the concentration of NPs is higher than 0.2 wt%, the texture of the smectic changes drastically, as shown in Fig. 6c. The FCDs and disclinations disappear, and the effect of surface curvature apparently vanishes. The smectic no longer presents a hybrid-aligned texture, suggesting that the anchoring conditions for the LC have changed at the boundaries. This could be induced by the accumulation of a large number of NPs at the surface of PDMS and coverslip due to the strong elastic forces of the LC expelling the NPs from the bulk. The presence of NPs at the boundaries could change the orientation of smectic layers at the double undulated surface to satisfy the surface anchoring of the NPs, which is degenerate planar, rather than the homeotropic anchoring of the PDMS. This result is similar to previous work with planar anchoring fluorosilane functionalized silica (F-SiO_2) NPs dispersed in semi-fluorinated smectic LC.[23] In that case, the NPs migrate to the boundaries and form monolayers capable of changing the alignment of smectic molecules. We believe that a similar mechanism is responsible for the change in smectic alignment in our system at high NP concentration. These results show that the TSA approach we propose in this study to organize NPs into reconfigurable 3D structures is inverted at high NP concentration: Rather than SmA LC defects directing the assembly of NPs, sufficiently concentrated NPs drastically alter the assembly of the SmA LC layers.

To gain insight into the concentration dependence of NP assembly in the SmA LC, we again employ LdG numerical free energy relaxation with adaptations to approximate a SmA configuration. NPs are introduced sequentially as small, spherical inclusions in the smectic-like LC configuration, with each NP's location chosen to minimize the LC free energy, with all previously inserted NPs held fixed. In these simulations, we consider NP concentrations ranging from 5 vol% to 17.5 vol%. These values are higher than the actual experimental concentrations, which are typically below 0.03 vol%, but were chosen to ensure that the NPs remain visible and resolvable within the limited size and resolution of the simulated system. This approach serves as a qualitative framework to conceptually support the experimental observations, rather than providing a direct quantitative comparison.

When planar anchoring is imposed on the NP surfaces, we observe a sequence of NP assembly behavior: the NPs first decorate the elliptical defect lines of the FCDs, then pack the flat surface, then decorating the hyperbolic defect lines, and next pack near the undulated surface, before finally filling the remainder of the LC bulk. This sequence of assembly is illustrated in Fig. 7a. These results are consistent with our experimental observations and support our hypothesis that, at low concentrations, NPs preferentially decorate the assembled defects. We also numerically investigate the effect of anchoring imposed on the surface of the NPs in the SI (Fig. S6), where we find that the ordered assembly of NPs is similarly observed in the case of homeotropic anchoring and no anchoring is imposed on the NP surface.

We can understand this assembly sequence based on the elastic energy cost of NPs, whose degenerate planar surface anchoring promotes bend distortions in the LC director field. As defect lines are regions of high free energy density, the LC free energy favors replacing portions of defect lines with NPs or colloidal particles, essentially reducing the energetic cost of these distortion sources by overlapping them.[78] The preference for NP assembly on the flat surface can be attributed to the higher anchoring strength on the flat surface compared to the undulated surface. The assembly of NPs on the flat surface relieves the energy cost of deviating from the imposed anchoring on the surface. Furthermore, the assembly of NPs at the boundaries reduces the total boundary area (including NP surfaces) thereby decreasing both the surface energy density and bulk elastic distortions.[79,80]

Examining the effect of NP concentration on the director field, we performed an additional LdG free energy minimization over the LC bulk, with NP locations held fixed at different volume fractions in the assembly sequence of Fig. 7a. At low NP concentration, the LC director near the double undulated surface primarily follows that surface's homeotropic

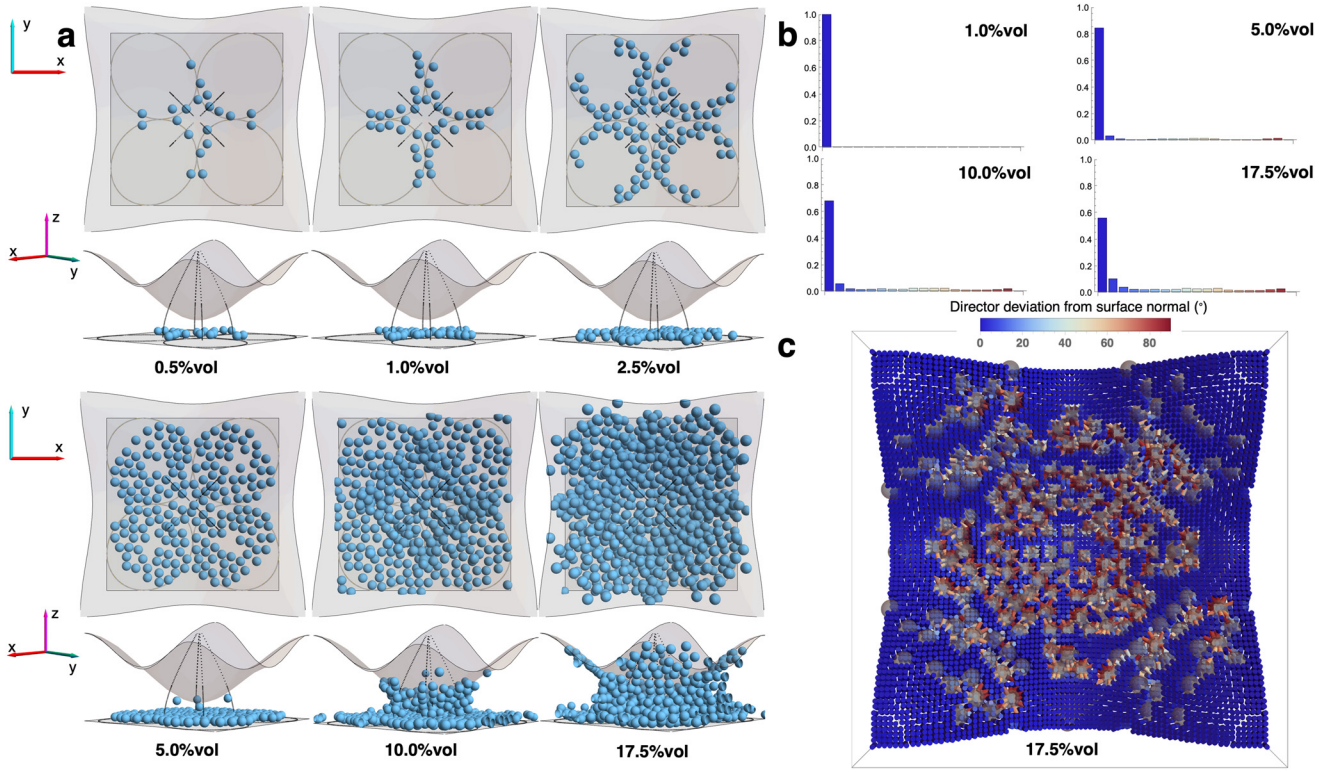

Fig. 7 NP assembly and effect of NPs on anchoring. (a) Sequential assembly of NPs with increasing concentration measured in %vol. Black lines show the positions of the elliptical and hyperbolic defects in the FCDs of the SmA phase. (b) The distribution of the deviation of the director field with respect to the undulated surface at different NP concentrations. (c) The director field close to the surfaces at 17.5%vol NP concentration. Gray spheres are the NPs found close to the surfaces.

anchoring condition. With increasing NP concentration, however, more sites near the double undulated surface are filled with NPs, resulting in an effective change in surface anchoring to the planar anchoring of the NP surfaces (Fig. 7b). This is further illustrated in Fig. 7c, where regions fully covered in NPs correspond to having ~90° deviation of the director from the surface normal of the undulated surface, *i.e.*, the effective anchoring in these regions is planar. In contrast, regions of the undulated surface with smaller NP coverage correspond to regions with a small deviation of the director from the surface normal. These results support our hypothesis that high NP concentrations cause the hybrid-aligned FCD texture to be replaced with approximately vertical layers having horizontal normal direction, similar to the bookshelf arrangement of layers observed previously with F-SiO_2 NPs in semi-fluorinated SmA LC.[23]

Conclusion

In this work, we demonstrated the benefits of using 3D printing to create curved confining geometries for a SmA LC mixture in order to control its defects and manipulate NP assembly. We demonstrate how this technique offers design flexibility and scalability, enabling the development of LC films with tailored properties. We also explain how 3D printing provides a powerful tool for engineering defects in smectic LCs. Additionally, we establish how these defects could be used as a template to assemble Au NPs and discuss the features of this approach.

Using LdG numerical modeling, we have gained insights into the influences of surface curvature and thermal history on the heterogeneous and highly multistable landscape of N-phase defect configurations under our geometrically structured confinement. To do so, we have introduced a novel, multi-step application of LdG free energy minimization to model the SmA–N transition from an initial state containing focal conic domains, together with the standard random initialization to model an I–N quench. We found that multistability of defect configurations is a consequence of the double-undulated surface geometry, and the location of defects—both boojums and disclination line endpoints—at the degenerate-planar anchoring surface is governed by the Gaussian curvature of the opposite, homeotropic-anchoring surface, a principle that holds promise for control over defects in more general confinement geometries. We showed that thermal history affects the N-phase defect configuration in terms of both its disorder or regularity and the types of point defects present. Furthermore, we used these simulations to gain deeper insight into the hierarchical assembly of NPs in the SmA phase, finding corroboration for a proposed mechanism of surface anchoring transformations at higher NP concentrations.

The technique of TSA could be adapted to various classes of functional nanomaterials useful in many technologies. For instance, it can be employed to enhance the performance of solar cells by incorporating quantum dots[81] or nanowires[82] into self-assembled FCDs. This may improve light absorption and charge transport within solar cells, leading to enhanced energy conversion efficiency. Another example is the fabrication of high-performance light-emitting devices.[83] By integrating luminescent nanomaterials into smectics, FCDs can be engineered to create ordered emission patterns. This control over defect structures could enable the production of devices with enhanced light extraction efficiency, color purity, and improved viewing angles.

Additionally, defect assemblies in LCs offer opportunities for biosensing applications.[84] By functionalizing the surfaces of nanomaterials with biomolecules or antibodies, FCDs can be used to capture and detect specific analytes or biological targets. The binding of these targets to the nanomaterials induces changes in the defect structures, which can be optically detected, enabling sensitive and label-free biosensing platforms. In each of these applications, the ability to control and manipulate LC defects provides a platform for the precise assembly and organization of nanomaterials, resulting in improved device performance, enhanced functionalities, and tailored properties.

Author contributions

M. A. G. and D. A. B. conceived of the presented idea. M. O., A. J. R., and M. A. G. collected and analyzed the experimental data. M. A. G. and T. M. O. designed and fabricated the 3D-printed double undulated substrates. J. B. D. M. G. and D. A. B. developed the theory and performed the numerical simulations. All authors discussed the results and contributed to the final manuscript.

Conflicts of interest

Authors have no conflict of interest to declare.

Data availability

All data supporting the findings of this study are available within the article and its SI.

The SI provides numerical simulations and experimental results supporting this study, including modeling of defect evolution in smectic liquid crystal at undulated surfaces, nanoparticle interactions with focal conic domains, and the influence of surface anchoring on nanoparticle assembly. See DOI: **https://doi.org/10.1039/d4nr02539c**.

Acknowledgements

M. A. G. and A. J. R. acknowledge UMass Boston for the support and the McNair fellowship. J. B. D. M. G. and D. A. B. acknowledge the donors of the American Chemical Society Petroleum Research Fund for partial support of this research (65254-DNI4). This work was supported in part by the National Science Foundation under grant numbers DMR-2338880 and DMR-2225543. Computational work was carried out at the Advanced Research Computing at Hopkins (ARCH) core facility (rockfish.jhu.edu), which is supported by the National Science Foundation grant number OAC 1920103.

References

1 J. Yin, Y. Huang, S. Hameed, R. Zhou, L. Xie and Y. Ying, *Nanoscale*, 2020, **12**, 17571–17589.
2 E. Pomerantseva, F. Bonaccorso, X. Feng, Y. Cui and Y. Gogotsi, *Science*, 2019, **366**, eaan8285.
3 V. Harish, D. Tewari, M. Gaur, A. B. Yadav, S. Swaroop, M. Bechelany and A. Barhoum, *Nanomaterials*, 2022, **12**, 457.
4 L. Gloag, M. Mehdipour, D. Chen, R. D. Tilley and J. J. Gooding, *Adv. Mater.*, 2019, **31**, 1904385.
5 Y. Li, Z. Wang, L. Sun, L. Liu, C. Xu and H. Kuang, *TrAC, Trends Anal. Chem.*, 2019, **113**, 74–83.
6 C. C. Chang, C. P. Chen, T. H. Wu, C. H. Yang, C. W. Lin and C. Y. Chen, *Nanomaterials*, 2019, **9**, 861.
7 L. Wang, M. H. Kafshgari, M. Meunier, L. Wang, M. H. Kafshgari and M. Meunier, *Adv. Funct. Mater.*, 2020, **30**, 2005400.
8 R. Fathima and A. Mujeeb, *J. Alloys Compd.*, 2021, **858**, 157667.
9 X. Zhao, H. Jin, J. Liu, J. Chao, T. Liu, H. Zhang, G. Wang, W. Lyu, S. Wageh, O. A. Al-Hartomy, A. G. Al-Sehemi, B. Fu, X. Zhao, G. Wang, B. Fu, H. Jin, J. Liu, J. Chao, T. Liu, H. Zhang, W. Lyu, S. Wageh and O. A. Al-Hartomy, *Laser Photonics Rev.*, 2022, **16**, 2200386.
10 H. Kang, D. Y. Kim and J. Cho, *ACS Omega*, 2023, **8**, 5885–5892.
11 R. A. Hughes, E. Menumerov and S. Neretina, *Nanotechnology*, 2017, **28**, 282002.
12 V. Auzelyte, V. Flauraud, V. J. Cadarso, T. Kiefer and J. Brugger, *Microelectron. Eng.*, 2012, **97**, 269–271.
13 J. C. Garno, Y. Yang, N. A. Amro, S. Cruchon-Dupeyrat, S. Chen and G. Y. Liu, *Nano Lett.*, 2003, **3**, 389–395.
14 M. Lee, J. Lin and T. Odom, *Angew. Chem.*, 2010, **122**, 3121–3124.
15 L. Yang, J. Wei, Z. Ma, P. Song, J. Ma, Y. Zhao, Z. Huang, M. Zhang, F. Yang and X. Wang, *Nanomaterials*, 2019, **9**, 1789.
16 L. Jiang, X. Chen, N. Lu and L. Chi, *Acc. Chem. Res.*, 2014, **47**, 3009–3017.
17 S. Kumar, P. Bhushan and S. Bhattacharya, *Energy, Environment, and Sustainability*, 2018, pp. 167–198.
18 J. Andreo, R. Ettlinger, O. Zaremba, Q. Peña, U. Lächelt, R. F. D. Luis, R. Freund, S. Canossa, E. Ploetz, W. Zhu, C. S. Diercks, H. Gröger and S. Wuttke, *J. Am. Chem. Soc.*, 2022, **144**, 7531–7550.

19 J. Y. Cheng, C. A. Ross, H. I. Smith and E. L. Thomas, *Adv. Mater.*, 2006, **18**, 2505–2521.
20 B. P. Isaacoff and K. A. Brown, *Nano Lett.*, 2017, **17**, 6508–6510.
21 X. Wang, D. S. Miller, E. Bukusoglu, J. J. D. Pablo and N. L. Abbott, *Nat. Mater.*, 2015, **15**(1), 106–112.
22 M. A. Gharbi, S. Manet, J. Lhermitte, S. Brown, J. Milette, V. Toader, M. Sutton and L. Reven, *ACS Nano*, 2016, **10**, 3410–3415.
23 A. Honglawan, D. S. Kim, D. A. Beller, D. K. Yoon, M. A. Gharbi, K. J. Stebe, R. D. Kamien and S. Yang, *Soft Matter*, 2015, **11**, 7367–7375.
24 E. Lee, Y. Xia, R. C. F. Jr, H.-N. Kim, M. A. Gharbi, K. J. Stebe, R. D. Kamien, R. J. Composto, S. Yang, E. Lee, Y. Xia, H. n Kim, M. A. Gharbi, R. J. Composto, S. Yang, R. C. F. Jr, K. J. Stebe and R. D. Kamien, *Adv. Mater.*, 2016, **28**, 2731–2736.
25 B. Senyuk, J. S. Evans, P. J. Ackerman, T. Lee, P. Manna, L. Vigderman, E. R. Zubarev, J. V. D. Lagemaat and I. I. Smalyukh, *Nano Lett.*, 2012, **12**, 955–963.
26 Y. Li, E. Prince, S. Cho, A. Salari, Y. M. Golestani, O. D. Lavrentovich and E. Kumacheva, *Proc. Natl. Acad. Sci. U. S. A.*, 2017, **114**, 2137–2142.
27 Y. H. Kim, D. K. Yoon, S. Jeong, O. D. Lavrentovich, H.-T. Jung, Y. H. Kim, D. K. Yoon, H. S. H. Jeong, T. Jung and O. D. Lavrentovich, *Adv. Funct. Mater.*, 2011, **21**, 610–627.
28 D. K. Yoon, M. C. Choi, Y. H. Kim, M. W. Kim, O. D. Lavrentovich and H. T. Jung, *Nat. Mater.*, 2007, **6**(11), 866–870.
29 D. Coursault, J. Grand, B. Zappone, H. Ayeb, G. Lévi, N. Félidj, E. Lacaze, D. Coursault, H. Ayeb, E. Lacaze, J. Grand, G. Lévi, N. Félidj and D. Zappone, *Adv. Mater.*, 2012, **24**, 1461–1465.
30 J. H. Kim, Y. H. Kim, H. S. Jeong, M. Srinivasarao, S. D. Hudson and H. T. Jung, *RSC Adv.*, 2012, **2**, 6729–6732.
31 F. Serra, M. A. Gharbi, Y. Luo, I. B. Liu, N. D. Bade, R. D. Kamien, S. Yang, K. J. Stebe, F. Serra, M. A. Gharbi, R. D. Kamien, Y. Luo, I. B. Liu, N. D. Bade, K. J. Stebe and S. Yang, *Adv. Opt. Mater.*, 2015, **3**, 1287–1292.
32 Y. H. Kim, D. K. Yoon, H. S. Jeong and H. T. Jung, *Soft Matter*, 2010, **6**, 1426–1431.
33 S. P. Do, A. Missaoui, A. Coati, D. Coursault, H. Jeridi, A. Resta, N. Goubet, M. M. Wojcik, A. Choux, S. Royer, E. Briand, B. Donnio, J. L. Gallani, B. Pansu, E. Lhuillier, Y. Garreau, D. Babonneau, M. Goldmann, D. Constantin, B. Gallas, B. Croset and E. Lacaze, *Nano Lett.*, 2020, **20**, 1598–1606.
34 H. Jeridi, J. de Dieu Niyonzima, C. Sakr, A. Missaoui, S. Shahini, A. Vlad, A. Coati, N. Goubet, S. Royer, I. Vickridge, M. Goldmann, D. Constantin, Y. Garreau, D. Babonneau, B. Croset, B. Gallas, E. Lhuillier and E. Lacaze, *Soft Matter*, 2022, **18**, 4792–4802.
35 C.-J. Hsu, L.-J. Lin, M.-K. Huang and C.-Y. Huang, *Crystals*, 2017, **7**, 287.
36 F. Ahmad, M. Luqman and M. Jamil, *Mol. Cryst. Liq. Cryst.*, 2021, **731**, 1–33.
37 A. K. Singh and P. Malik, *Liq. Cryst.*, 2022, **49**, 864–874.
38 F. V. Podgornov, M. Gavrilyak, A. Karaawi, V. Boronin and W. Haase, *Liq. Cryst.*, 2018, **45**, 1594–1602.
39 K. Pal, A. Si, G. S. El-Sayyad, M. Abd Elkodous, R. Kumar, A. I. El-Batal, S. Kralj and S. Thomas, *Crit. Rev. Solid State Mater. Sci.*, 2021, **46**, 385–449.
40 A. Si, G. Z. Kyzas, K. Pal and F. G. de Souza Jr., *J. Mol. Struct.*, 2021, **1239**, 130518.
41 J. M. Ok, Y. H. Kim, T. Y. Lee, H. W. Yoo, K. Kwon, W. B. Jung, S. H. Kim and H. T. Jung, *Langmuir*, 2016, **32**, 13418–13426.
42 D. S. Kim, A. Honglawan, S. Yang and D. K. Yoon, *ACS Appl. Mater. Interfaces*, 2017, **9**, 7787–7792.
43 Y. Shen and I. Dierking, *Appl. Sci.*, 2019, **9**, 2512.
44 A. Suh, H. Ahn, T. J. Shin and D. K. Yoon, *J. Mater. Chem. C*, 2019, **7**, 1713–1719.
45 M. J. Shin and D. K. Yoon, *Materials*, 2020, **13**, 5466.
46 Y. H. Kim, D. K. Yoon, M.-C. Choi, H. S. Jeong, M. W. Kim, O. D. Lavrentovich and H.-T. Jung, *Langmuir*, 2009, **25**, 1685–1691.
47 A. Honglawan, D. A. Beller, M. Cavallaro, R. D. Kamien, K. J. Stebe and S. Yang, *Adv. Mater.*, 2011, **23**, 5519–5523.
48 A. Honglawan, D. A. Beller, M. Cavallaro Jr, R. D. Kamien, K. J. Stebe and S. Yang, *Proc. Natl. Acad. Sci. U. S. A.*, 2013, **110**, 34–39.
49 D. A. Beller, M. A. Gharbi, A. Honglawan, K. J. Stebe, S. Yang and R. D. Kamien, *Phys. Rev. X*, 2014, **3**, 041026.
50 M. A. Gharbi, I. B. Liu, Y. Luo, F. Serra, N. D. Bade, H. N. Kim, Y. Xia, R. D. Kamien, S. Yang and K. J. Stebe, *Langmuir*, 2015, **31**, 11135–11142.
51 R. S. Preusse, E. R. George, S. A. Aghvami, T. M. Otchy and M. A. Gharbi, *Soft Matter*, 2020, **16**, 8352–8358.
52 R. Parthasarathy, C. H. Yu and J. T. Groves, *Langmuir*, 2006, **22**, 5095–5099.
53 L. Guillemeney, L. Lermusiaux, G. Landaburu, B. Wagnon and B. Abécassis, *Commun. Chem.*, 2022, **5**(1), 1–11.
54 K. P. Browne and B. A. Grzybowski, *Langmuir*, 2011, **27**, 1246–1250.
55 H. Liu, Y. Zong and K. Zhao, *Langmuir*, 2021, **37**, 9264–9268.
56 M. Cavallaro, L. Botto, E. P. Lewandowski, M. Wang and K. J. Stebe, *Proc. Natl. Acad. Sci. U. S. A.*, 2011, **108**, 20923–20928.
57 H. Xiang, K. Shin, T. Kim, S. Moon, T. J. Mccarthy and T. P. Russell, *J. Polym. Sci., Part B: Polym. Phys.*, 2005, **43**, 3377–3383.
58 D. S. Kim and D. K. Yoon, *J. Inf. Disp.*, 2017, **19**, 7–23.
59 T. Lopez-Leon and A. Fernandez-Nieves, *Colloid Polym. Sci.*, 2011, **289**, 345–359.
60 P. W. Ellis, D. J. Pearce, Y. W. Chang, G. Goldsztein, L. Giomi and A. Fernandez-Nieves, *Nat. Phys.*, 2017, **14**(1), 85–90.
61 B. W. Pearre, C. Michas, J. M. Tsang, T. J. Gardner and T. M. Otchy, *Addit. Manuf.*, 2019, **30**, 100887.
62 P. G. de Gennes and J. Prost, *The Physics of Liquid Crystals*, Clarendon Press, 1995.

63 M. Kleman and O. D. Lavrentovich, *Soft matter physics*, Springer, 2003.
64 A. Rapini and M. Papoular, *J. Phys. Colloq.*, 1969, **30**, C1–27.
65 M. Nobili and G. Durand, *Phys. Rev. A*, 1992, **46**, R6174–R6177.
66 J.-B. Fournier and P. Galatola, *Europhys. Lett.*, 2005, **72**, 403–409.
67 A. Suh, M. J. Gim, D. Beller and D. K. Yoon, *Soft Matter*, 2019, **15**, 5835–5841.
68 M. J. Gim, D. A. Beller and D. K. Yoon, *Nat. Commun.*, 2017, **8**, 15453.
69 M. Ravnik and S. Žumer, *Liq. Cryst.*, 2009, **36**, 1201–1214.
70 M. Cestari and A. Ferrarini, *Soft Matter*, 2009, **5**, 3879–3887.
71 D. J. Ternet, R. G. Larson and L. G. Leal, *Rheol. Acta*, 1999, **38**, 183–197.
72 K. P. Zuhail, S. Čopar, I. Muševič and S. Dhara, *Phys. Rev. E: Stat., Nonlinear, Soft Matter Phys.*, 2015, **92**, 52501.
73 K. P. Zuhail, P. Sathyanarayana, D. Seč, S. Čopar, M. Skarabot, I. Muševič and S. Dhara, *Phys. Rev. E: Stat., Nonlinear, Soft Matter Phys.*, 2015, **91**, 30501.
74 A. M. Turner, V. Vitelli and D. R. Nelson, *Rev. Mod. Phys.*, 2010, **82**, 1301.
75 P. W. Ellis, D. J. Pearce, Y.-W. Chang, G. Goldsztein, L. Giomi and A. Fernandez-Nieves, *Nat. Phys.*, 2018, **14**, 85–90.
76 L. Tran, M. O. Lavrentovich, D. A. Beller, N. Li, K. J. Stebe and R. D. Kamien, *Proc. Natl. Acad. Sci. U. S. A.*, 2016, **113**, 7106–7111.
77 M. Tasinkevych, N. M. Silvestre and M. M. T. da Gama, *New J. Phys.*, 2012, **14**, 073030.
78 O. D. Lavrentovich, *Soft Matter*, 2014, **10**, 1264–1283.
79 R. Bitar, G. Agez and M. Mitov, *Soft Matter*, 2011, **7**, 8198.
80 C. Blanc, D. Coursault and E. Lacaze, *Liq. Cryst. Rev.*, 2013, **1**, 83–109.
81 S. Phetsang, S. Nootchanat, C. Lertvachirapaiboon, R. Ishikawa, K. Shinbo, K. Kato, P. Mungkornasawakul, K. Ounnunkad and A. Baba, *Nanoscale Adv.*, 2020, **2**, 2950–2957.
82 Y. Zhang and H. Liu, *Crystals*, 2019, **9**, 87.
83 Y. Yang, Y. Zheng, W. Cao, A. Titov, J. Hyvonen, J. R. Manders, J. Xue, P. H. Holloway and L. Qian, *Nat. Photonics*, 2015, **9**, 259–266.
84 S. Huang, Y. Song, Z. He, J.-R. Zhang and J.-J. Zhu, *Analyst*, 2021, **146**, 2807–2817.